JOURNAL OF SYNCHROTRON RADIATION
ISSN 1600-5775

X-ray fluorescence at nanoscale resolution for multicomponent layered structures: a solar cell case study

Bradley M. West,[a] Michael Stuckelberger,[a] April Jeffries,[b] Srikanth Gangam,[a] Barry Lai,[c] Benjamin Stripe,[c,d] Jörg Maser,[c] Volker Rose,[c,e] Stefan Vogt[c] and Mariana I. Bertoni[a,b]*

[a]School of Electrical, Computer, and Energy Engineering, Arizona State University, 551 E Tyler Mall, Tempe, AZ 85281, USA, [b]School for Engineering of Matter, Transport, and Energy, Arizona State University, 551 E Tyler Mall, Tempe, AZ 85281, USA, [c]Advanced Photon Source, Argonne National Laboratory, Lemont, IL 60439, USA, [d]Sigray, 5750 Imhoff Drive, Suite 1, Concord, CA 94520, USA, and [e]Center for Nanoscale Materials, Argonne National Laboratory, Lemont, IL 60439, USA. *Correspondence e-mail: bertoni@asu.edu

Received 1 December 2015
Accepted 6 October 2016

Edited by A. Momose, Tohoku University, Japan

Keywords: thin film characterization; X-ray fluorescence; CIGS; multilayered structure; solar cell.

The study of a multilayered and multicomponent system by spatially resolved X-ray fluorescence microscopy poses unique challenges in achieving accurate quantification of elemental distributions. This is particularly true for the quantification of materials with high X-ray attenuation coefficients, depth-dependent composition variations and thickness variations. A widely applicable procedure for use after spectrum fitting and quantification is described. This procedure corrects the elemental distribution from the measured fluorescence signal, taking into account attenuation of the incident beam and generated fluorescence from multiple layers, and accounts for sample thickness variations. Deriving from Beer–Lambert's law, formulae are presented in a general integral form and numerically applicable framework. The procedure is applied using experimental data from a solar cell with a $Cu(In,Ga)Se_2$ absorber layer, measured at two separate synchrotron beamlines with varied measurement geometries. This example shows the importance of these corrections in real material systems, which can change the interpretation of the measured distributions dramatically.

1. Introduction

The construction of third-generation synchrotron facilities and their continuous upgrade over the past few decades have increased the available photon flux and beam coherence by orders of magnitude. This dramatic increase in brilliance of synchrotrons pushes research towards new horizons by enabling two major developments. First, the high coherence allows the use of lens-less imaging techniques such as ptychography (Dierolf *et al.*, 2010) for two- and three-dimensional reconstructions of features that are smaller than the beam spot size. Second, high-resolution optics such as multilayered Laue lenses and Fresnel zone plates were developed, enabling X-ray beam spot sizes (and therefore, two-dimensional mapping) down to 11 nm in nanoprobe beamlines (Chu *et al.*, 2008; Huang *et al.*, 2013).

X-ray fluorescence (XRF) measures elemental concentrations with a sensitivity up to parts per million (Sakdinawat & Attwood, 2010). Core-level electrons are excited by exposing a sample to a high-energy X-ray source with an incident photon energy higher than the electron binding energy. When an electron in a higher shell relaxes to the unoccupied lower energy state, a fluorescent photon is emitted. These photons have a characteristic energy based on the element excited,

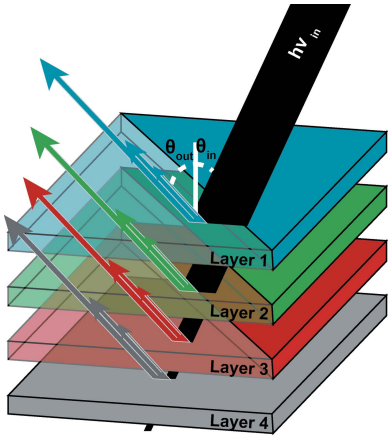

and, by measuring the energy of fluorescence photons, constituent elements can be determined. Quantification of these elements is achieved by comparing the number of collected photons at a given energy to a well quantified standard. This technique has been used in a variety of applications for high-resolution elemental imaging. For example, Paunesku *et al.* (2006) analysed the accumulation of metals in human cells associated with the development or inhibition of diseases and tomographic XRF has been utilized to develop a three-dimensional reconstruction of elemental distributions in freshwater diatoms (Jonge *et al.*, 2010). In silicon solar cells, XRF was used to investigate the presence of transition metal impurities surrounding dislocations which are correlated to decreased conversion efficiency (Bertoni *et al.*, 2011). Fuel cells membrane assemblies were investigated using XRF for the effects of contamination with Ca and Cs (Kienitz *et al.*, 2011). It has also been used to investigate pigments in paintings and ancient texts where multiple layers are present, making accurate elemental quantification difficult (Bergmann, 2007; Casadio & Rose, 2013). Terrestrial and extraterrestrial samples have been investigated with XRF to trace metastable phases (Bleuet *et al.*, 2008). Additionally, XRF has been used to investigate composition variations between grains and grain boundaries in polycrystalline thin film solar cells (West *et al.*, 2015). Grazing-incidence XRF measurements (GIXRF) (Streeck *et al.*, 2013), and a combination of GIXRF and ion beam analyses (Karydas *et al.*, 2015), have also been used to calculate depth-dependent gradients.

The combination of XRF with a synchrotron nanoprobe beamline enables the measurement of elemental distributions with higher sensitivity and spatial resolution than other techniques such as secondary ion mass spectroscopy or XRF with a laboratory X-ray source. This combination also enables the structural and elemental characterization of a whole class of materials with sub-micrometre-sized features. This is particularly interesting for thin films deposited by sputtering, evaporation or chemical vapour deposition, where often multicrystalline materials result with crystallite sizes well below tens of micrometres.

Many applications of XRF in the past relied on hard X-rays to detect small quantities or even traces of an element in a low-absorption matrix (*e.g.* Si or organic materials) (Vyvenko *et al.*, 2004; Buonassisi *et al.*, 2006; Paunesku *et al.*, 2006; Bertoni *et al.*, 2011). However, challenges arise in the XRF analysis of thin films (with a thickness on the order of a few micrometres) that consist of heavier elements, including

(i) Layers of interest buried within a complex stack of several layers, including substrates, that all can contain XRF-active elements. How does one distinguish XRF from different layers?

(ii) Quantifying minor composition fluctuations, if the elements of interest are the majority components, not traces in an X-ray transparent matrix, and the constituent layer has significant thickness variations.

Although the physics governing these challenges has been very well described (De Boer, 1990; Grieken & Markowicz, 2002; Brunetti *et al.*, 2015), and some aspects have already been implemented in X-ray data analysis packages such as *GeoPIXIE* and *PyMCA* (Ryan *et al.*, 2005; Solé *et al.*, 2007; Schoonjans *et al.*, 2012), it is still important to address the practical implementation of these analyses towards high spatial resolution mapping of real material systems, such as thin film solar cells. We note the challenges and potential sources of error associated with correcting data for materials with lateral composition variations, thickness variations and depth-dependent composition variations. We also show the potential for misinterpretation if these factors are not properly addressed.

With this as the motivation for the present study, we build upon the analysis made by Mainz and Klenk, wherein they utilized a polychromatic, unfocused source to measure a single film with a depth-dependent composition gradient (Mainz & Klenk, 2011). We expand the formalism to include the corrections for a monochromatic, highly focused X-ray beam, a multilayered structure and thickness variations which become much more critical as spatial resolution increases. In the following sections, we describe this generalized user-friendly procedure to apply corrections to XRF data for any material system after spectrum fitting and quantification. Walking through the corrections step-by-step using $Cu(In,Ga)Se_2$ (CIGS) solar cells with sub-micrometer-sized features as an example, we highlight the importance of the corrections by showing that uncorrected data can suggest opposite trends from corrected data and identify sources of uncertainty in the analysis.

2. Procedure

2.1. Fitting of raw data and thickness correction

Mapping during XRF measurements, by scanning the sample in X and Y directions, produces a full energy spectrum for each measurement spot (Fig. 1*a*). Fig. 1(*b*) shows the x–y distribution in units of counts of an element of interest (Cu), by isolating the corresponding peak from the per-pixel spectrum. Prior to correcting the data for absorption losses, the XRF spectra are fitted for the quantification of different elements (Fig. 1*c*). To ensure an accurate fit, branching ratios need to be well defined. Branching ratios of X-ray fluorescence from K lines are tabulated in the literature and well studied (Krause, 1979); however, L-line branching ratios tend to vary as a function of excitation energy (Hubbell *et al.*, 1994). Therefore, it may be necessary to measure L-edge branching ratios for a specific experiment. From the fit, the intensities of the peaks are isolated and compared with the intensities of a well quantified standard that is measured under the exact same geometry as the sample (AXO Dresden, 2015). Applying a calibration curve to the elements of known concentration in the standard gives access by interpolation/extrapolation to the relative XRF signal of different elements that are not contained in the standard but may be in the sample. The data are processed in this fashion, pixel by pixel in each map collected, resulting in elemental maps in units of weight per area (Fig. 1*d*). To accurately quantify the elemental compo-

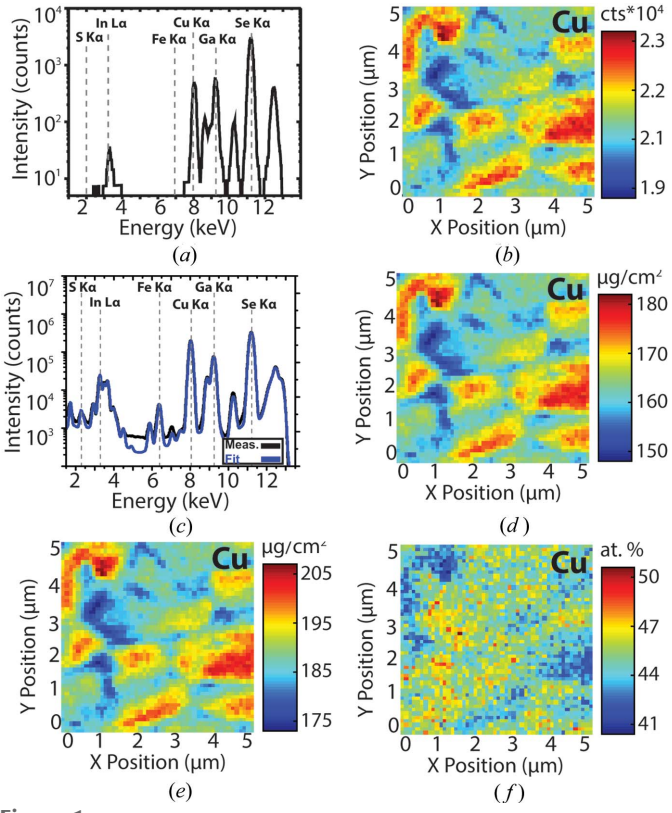

Figure 1
Diagram showing the XRF data flow to quantify a copper map measured from a CIGS solar cell. Starting with the single spectra found in each pixel (*a*), going to the two-dimensional unfitted XRF map (*b*), a fit of the integrated spectrum (*c*), and proceeding through quantification (*d*), absorption correction (*e*) and thickness correction (*f*).

sition of a sample with multiple layers of materials with non-negligible absorption coefficients, the data should be corrected for attenuation (Fig. 1*e*). If the sample is not perfectly flat, surface topology has an impact on the data collected. In most cases, one is interested in compositional variations and thickness variations can be readily misinterpreted as compositional variations. To account for thickness variations, mass-based concentrations can be converted to atomic percentages by dividing an elemental map by the density-weighted sum of all elements in the layer of interest, pixel by pixel, isolating changes in stoichiometry (Fig. 1*f*). An alternative approach could involve measuring the thickness variations directly (*e.g.* by atomic force microscopy) and conducting XRF on the same area or combining XRF scans with tomographic information (Hu *et al.*, 2014).

2.2. Correcting losses due to attenuation

Beer–Lambert's law (Beer, 1852) describes the intensity decay of light in matter:

$$I/I_0 = \exp(-\mu L), \tag{1}$$

where I/I_0 represents the fractional intensity of transmitted light, μ is the attenuation coefficient in cm^{-1} and L (cm) is the path length of the light in the material. The attenuation coefficient is the product of the density ρ ($\mathrm{g\,cm}^{-3}$) and the capture cross section σ ($\mathrm{cm}^2\,\mathrm{g}^{-1}$). For many material systems, μ is well known and tabulated; however, for systems where μ is not well characterized, it can be calculated from capture cross section databases available for most elements through the National Institute of Standards and Technology (Berger *et al.*, 2013) and by using a sample-specific material density. Beer–Lambert's law in its current form is useful for describing the intensity decay of visible light or X-rays propagating through a single uniform medium to a certain depth or thickness. It should be expanded to account for: multiple layers, such as stacks used in thin film solar cells, depth-dependent composition variations, attenuation of both the incident beam and the generated fluorescent photons, and average attenuation as fluorescence occurs continuously throughout the sample thickness. The following formulation is intended to serve as an experimental approach to correct for attenuation and self-absorption of the exciting photons and photons at a fixed fluorescence energy, which can be repeated and applied to each element of interest. Note that an accurate representation of the attenuation of all fluorescence generated within the layer stack will require a more complete formalism which accounts for the probability for fluorescence to occur, secondary fluorescence effects, and a three-dimensional model which accounts for the 4π generation of fluorescence.

Fig. 2 depicts these effects in a multicomponent layered structure. The incident X-ray beam, hitting the sample surface under the angle θ_{in}, shown in black, is attenuated through each layer of the stack. The multiple arrows exiting each layer represent the fluorescent photons with varied energies that are also attenuated as they exit the stack. The increased

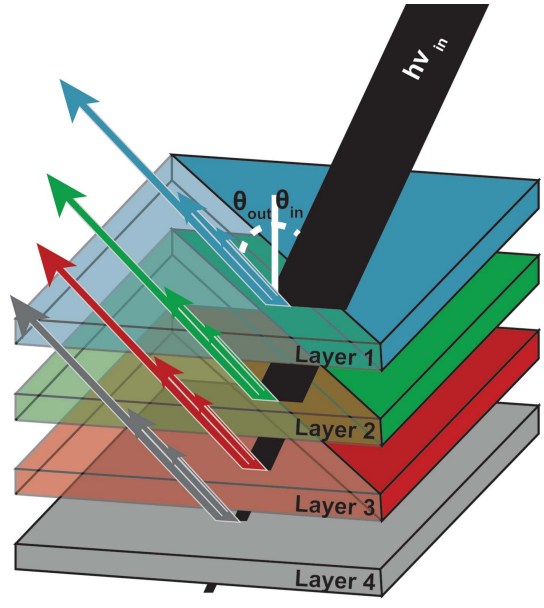

Figure 2
Diagram showing the propagation and attenuation of high-energy photons entering the sample stack and fluorescent photons exiting towards the detector. Each multicomponent layer generates photons of different energies that have different attenuation coefficients in each layer. The multicomponent nature of each layer is represented with multiple arrows exiting each layer.

attenuation throughout the thickness leads to increased XRF signal from the sample surface, and decreased signal from the bulk and back of the sample. While the fluorescence process is isotropic, we only need to consider those photons that are emitted under the angle θ_{out} such that they can reach the fluorescence detector. These two angles impact the beam path length and ultimately the measured fluorescence intensity.

To account for multiple layers and depth-dependent composition variations, μ is no longer constant with light path L. The light path can be divided into small sub-layers of length (Δl) over which μ can be assumed constant. The product of equation (1) over each of these sub-layers is the total intensity decay and the exponent can be treated as a summation shown in equation (2), where N is the total number of layers in the structure and $\mu(l_i)$ is the attenuation coefficient at length l_i,

$$\begin{aligned} I_T/I_0 &= \exp(-\mu L) \\ &= \exp(-\mu_1 \Delta l)\exp(-\mu_2 \Delta l)\ldots\exp(-\mu_n \Delta l) \\ &= \exp\left[\sum_{i=1}^{N} -\mu(l_i)\Delta l\right]. \end{aligned} \quad (2)$$

By taking the limit of the summation as N approaches infinity, the expression can be re-written as a definite integral from the top of the layer stack (0), where the incident beam hits the sample, to the total light path length. This is shown in equation (3):

$$\frac{I_T}{I_0} = \exp\left[\lim_{N\to\infty}\sum_{i=1}^{N} -\mu(l_i)\Delta l\right] = \exp\left[\int_0^L -\mu(l)\,\mathrm{d}l\right]. \quad (3)$$

This equation describes the light path of the incident beam. In addition, the generated fluorescence is attenuated in a similar way. The measurement geometry and thickness of the sample impacts the length of both light paths and is accounted for in equation (4) in terms of the sample thickness. We introduced the terms $L = T\cos(\theta_{in})^{-1}$ for the incident beam and $L = T\cos(\theta_{out})^{-1}$ for the fluorescence, to treat the light path in terms of thickness and measurement geometry:

$$\frac{I_T}{I_0} = \exp\left[\int_0^{T\cos(\theta_{in})^{-1}} -\mu_{in}(t)\,\mathrm{d}t + \int_0^{T\cos(\theta_{out})^{-1}} -\mu_{out}(t)\,\mathrm{d}t\right]. \quad (4)$$

Equation (4) describes the intensity decay from the incident beam (μ_{in}) and generated fluorescence of a particular element of interest (μ_{out}) at a given depth t and sample thickness T, as the ratio of the intensities of the specified elemental fluorescence (I_T) and the incident beam intensity (I_0). It should be noted that this equation just describes the attenuation of the X-rays, and the probability of fluorescence to occur is taken into account during the fitting and quantification of the spectrum. Effects such as secondary fluorescence are not included and assumed to be negligible for the purpose of this analysis. For a detailed discussion on how to take into account secondary fluorescence when necessary, see De Boer (1990). As mentioned previously, the detector measures the number and energy of photons collected, and photons generated from different sample depths are treated equally. Because, fluorescence occurs continuously throughout the sample thickness, the average attenuation caused by the stack needs to be calculated. This is shown in equation (5):

$$\begin{aligned} \frac{I}{I_0} &= \frac{1}{T}\int_0^T \frac{I_T}{I_0}\,\mathrm{d}t \\ &= \frac{1}{T}\exp\left[\int_0^{T\cos(\theta_{in})^{-1}} -\mu_{in}(t)\,\mathrm{d}t + \int_0^{T\cos(\theta_{out})^{-1}} -\mu_{out}(t)\,\mathrm{d}t\right]\mathrm{d}t. \end{aligned} \quad (5)$$

The resulting value I/I_0 is a value between 0 and 1 representing the average intensity decrease of detected fluorescence compared with the incident beam intensity. Although mathematically accurate, this equation is, in general, not analytically solvable due to the depth dependence of μ_{in} and μ_{out}. It can be simplified by assuming a finite layer thickness (Δt) over which $\mu(t)$ can be assumed constant. This is shown in equation (6),

$$\frac{I}{I_0} = \frac{1}{T}\sum_{N=1}^{T}\exp\left\{\sum_{i=1}^{N}\left[\frac{-\mu_{in}(t_i)}{\cos(\theta_{in})}\Delta t_i + \frac{-\mu_{out}(t_i)}{\cos(\theta_{out})}\Delta t_i\right]\right\}. \quad (6)$$

Once the losses are calculated for each of the elements of interest, every pixel value in the XRF map is then divided by I/I_0 to correct for the losses described in this section. Additionally, I/I_0 in the final formulation presented here should be considered as an effective correction factor taking into account attenuation of exciting and fluorescent radiation through capping layers, as well as self-attenuation within a layer of interest. It should be noted again that this analysis assumes a radiation-free attenuation of generated XRF photons. These secondary effects are assumed negligible in the following case, although can have an impact.

Table 1
Measurement geometries and beam information for two separate beamlines at APS used to measure XRF on CIGS solar cells.

Beamline	Beam energy (keV)	Beam angle (θ_{in}) (°)	Detector angle (θ_{out}) (°)	Spot size (nm)
APS 2-ID-D	10.4	0	77	185
APS 26-ID-C	10.4	15	75	40–50

3. Experimental setup

The process described in §2 was tested on a Cu(In,Ga)Se_2 (CIGS) solar cell measured at two different beamlines [2-ID-D (Yun *et al.*, 1999) and 26-ID-C (Winarski *et al.*, 2012)] at the Advanced Photon Source (APS) at Argonne National Laboratory. The measurement parameters are described in Table 1.

The device structure is similar to that shown in Fig. 2. Layer 1 corresponds to intrinsic ZnO and ZnO:Al (150 nm), Layer 2 is CdS (50 nm), Layer 3 is CIGS with a Ga/(Ga+In) ratio of 0.3 (1.6 µm), and Layer 4 is Mo (700 nm) deposited on a soda lime glass substrate. A more detailed discussion of sample preparation and device structure conducted at the National Renewable Energy Laboratory (NREL) can be found in

(Contreras *et al.*, 1994). This device exhibits a typical V-shaped grading through the CIGS layer with high gallium content at the front, the back and lower in the middle. As reference, an AXO thin film standard was used, containing the elements Pb, La, Pd, Mo, Cu, Fe and Ca, on silicon nitride. The data were quantified and fitted using *MAPS* software developed at the APS (Vogt, 2003; Vogt *et al.*, 2003). Fluorescence was detected on a Vortex-ME4 four-element energy-dispersive silicon drift detector at beamline 26-ID-C and on a Vortex-EM/ASIC single-element energy-dispersive silicon drift detector at 2-ID-D.

4. Results

Fig. 3 shows typical XRF maps collected at APS 2-ID-D. Uncorrected data refer to the XRF data not treated for absorption losses, depth-dependent composition variations or thickness variations, and corrected data refer to the data after correcting for these factors. The maps are 5 µm × 5 µm with 100 nm × 100 nm pixel size, taken with a 1 s dwell time. Selenium (Se *K* edge = 12.66 keV) was not collected during this run to enhance sensitivity to the cations, Cu, Ga and In.

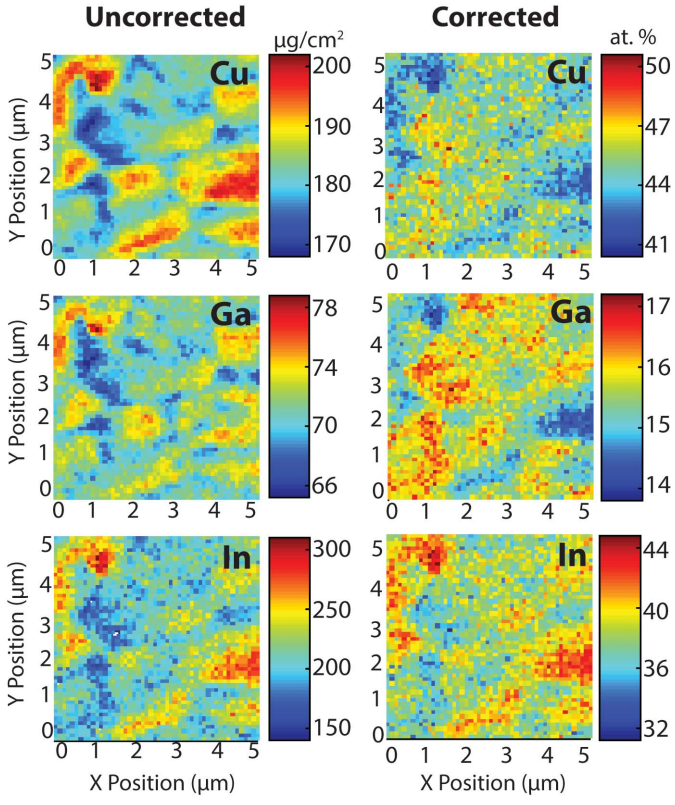

Figure 3
X-ray fluorescence maps taken at APS 2-ID-D. Left-hand panels show the uncorrected data after quantification with a reference standard (in µg cm^{-2}) and right-hand panels show the same maps after correction for thickness and attenuation of incident and fluorescence photons (in at.%). Note that the counter-intuitive change from high to low concentration observed in the copper and gallium maps is the result of the thickness correction. The apparent high concentration in uncorrected maps is due to increased sample thickness in the center of grains, although with respect to stoichiometry, these regions are copper/gallium poor.

After correcting for thickness variations, attenuation losses and depth-dependent composition grading, the maps look quite different. The top left corner appears to have the highest concentration of all copper, gallium and indium across the map. However, after thickness correction, described previously, it can be seen that this region is actually copper and gallium poor, and indium rich. This highlights that the concentration variations observed in the uncorrected map are largely due to thickness variations because the compositional inhomogeneity of the sample is smaller in magnitude than variations due to surface roughness. This leads to a significantly different interpretation of the XRF data than would have resulted using uncorrected maps. It should be noted that the thickness-corrected XRF maps appear much noisier than the uncorrected images. This is mainly due to the noise associated with the indium channel. The incident beam energy of 10.4 keV is much higher than the indium *L*1-edge (4.34 keV), leading to decreased sensitivity to variations in indium.

Fig. 4 shows XRF maps for a CIGS device measured at two different APS beamlines. The uncorrected maps show the fitted quantified data in µg cm^{-2}. The large difference in the quantification of uncorrected maps should be noted. For example, the measurement taken at 2-ID-D shows a maximum copper concentration of 205 µg cm^{-2}, whereas the measurement taken at 26-ID-C shows a maximum of 105 µg cm^{-2}. After application of the corrections to account for the different attenuation losses between the two geometries and normalized for thickness, the concentration measured in atomic percent shows better agreement between the two

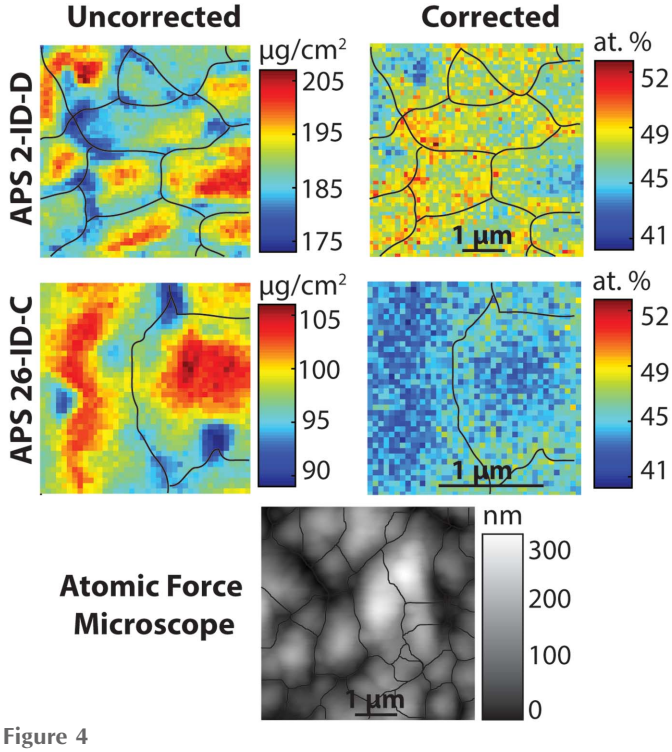

Figure 4
Copper X-ray fluorescence maps of the same CIGS sample, taken at two beamlines with different geometries and beam intensity. AFM map with delineated grain boundaries presents a comparison with the grain sizes obtained using the watershed technique.

beamlines. The remaining 4% difference between the average atomic percentages of copper for the two maps can be attributed to the inhomogeneities in the sample and standards used to quantify the raw XRF data and to the fact that two different standards were used to quantify these data sets.

The black lines on the images depict the position of the grain boundaries and are the result of image processing by flooding watershed (Tsukahara *et al.*, 2008). This technique has been successfully applied to particle segmentation in X-ray tomography and is well established to separate grains (Delaney *et al.*, 2010; Mukhopadhyay & Peixinho, 2011; Fu *et al.*, 2012). We have also verified its accuracy by comparing AFM and SEM images on the same area measured using XRF. A detailed discussion will be given by West *et al.* (2016). A comparison of the AFM and XRF images in Fig. 4, taken on the same sample, reveals similar grain sizes (1–2 µm) and shapes. This suggests that the flooding watershed technique is an appropriate method to identify grain boundaries in our case and it confirms that we are not limited by beam spot size for grain identification.

5. Discussion and conclusions

Potential sources of error and uncertainty should be taken into consideration when calculating correction factors for non-ideal samples using this method. To determine the impact of uncertainty in the grading profile, I/I_0 was calculated for Cu $K\alpha$, Ga $K\alpha$, In $L\alpha_1$ and Se $K\alpha$ fluorescence as a function of CIGS layer thickness for five different [Ga]/[Ga+In] grading profiles. These values were calculated using the device structure described previously, with a beam energy of 10.4 keV and the sample-to-detector geometry used at 26-ID-C. It should be noted that the following results describe not only the attenuation from ZnO and CdS layers but self-attenuation in the CIGS layer as well. The thickness variations shown are only for the CIGS layer, and the ZnO and CdS thickness are kept constant. These curves are shown in Fig. 5 and the subset in Fig. 5(*d*) shows the grading profiles. The flat profile is not shown, but represents a uniform composition throughout the film thickness. Each profile has the same average [Ga]/[Ga+In] ratio of 0.5. It can be seen that as layer thickness increases, I/I_0 for each element decreases. As the layer thickness approaches 0, I/I_0 values do not reach 1. This is due to the attenuation from the CdS and ZnO layers. It can be seen that for CIGS under these measurement conditions, variations in the grading profile have a small impact of <1% for typical layer thickness ∼2 µm but can reach closer to 2% for Cu and Se for thicker layers. The 'V', 'A' and flat grading profiles show negligible change between them, but slight variations are observed for the linear 'up' and 'down' profiles. The 'down' profile results in less copper and gallium attenuation compared with the 'up' profile and the opposite was observed for indium and selenium. For indium and gallium this is due to the fact that the highest concentration of these elements is closest to the surface, for their respective grading profiles, resulting in less total signal attenuation from the CIGS bulk. Selenium fluorescence is strongly absorbed by Ga and by having a higher

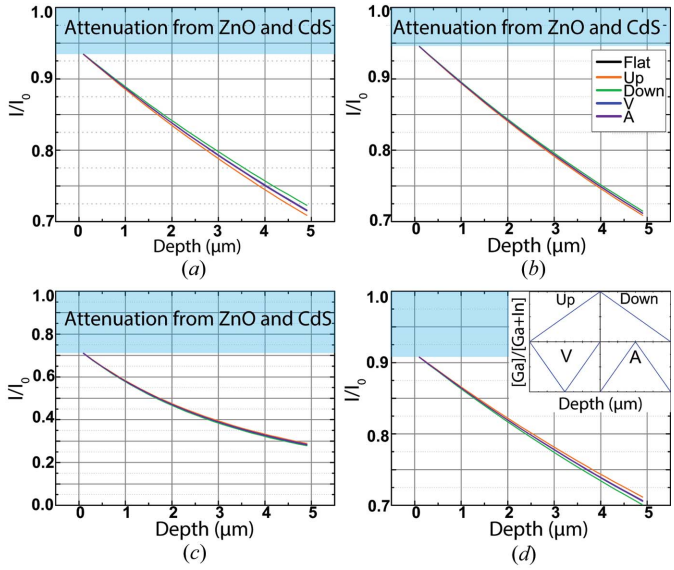

Figure 5
I/I_0 values for (*a*) copper, (*b*) gallium, (*c*) indium and (*d*) selenium as a function of CIGS layer thickness for five different grading profiles all assuming the same average film composition. The insets in (*b*) and (*d*) refer to all panels. The difference in scale for (*c*) should be noted when compared with (*a*), (*b*) and (*d*).

gallium concentration at the surface there is a slight decrease in the selenium I/I_0. The same justification can be made for copper fluorescence being more affected by a high indium concentration at the surface.

Using the same geometry, layer stack, beam energy and assuming a flat grading profile, we have also examined the impact of surface roughness on I/I_0. It is clear from Fig. 5 and the derivation explained earlier [§2.2] that thickness has a large impact on beam and fluorescence attenuation. Fig. 6 shows the change in I/I_0 for copper, gallium, indium and selenium with varying layer thickness and surface roughness (from 10% to 100% of the film thickness with the black reference line representing no surface roughness). The two dashed lines for each surface roughness represent maximum change in I/I_0 for a positive and negative thickness variation. The distance between these lines for a given thickness can represent the uncertainty in the correction factor. CIGS films investigated typically have a surface roughness between 150 and 200 nm for films that are between 1.5 and 2 µm thick, leading to ∼10% surface roughness. This leads to ∼2% uncertainty for Cu, Ga and Se $K\alpha$ lines and ∼5% uncertainty for indium. As total film thickness increases the uncertainty in the correction factor for a given surface roughness also increases. For very rough samples with materials that have high attenuation coefficients, the uncertainty in the correction can be quite large if surface roughness is not considered.

It can be seen that there is a large uncertainty for elements with high attenuation coefficients in rough films. To reduce this uncertainty and bring I/I_0 as close to 1 as possible, the path lengths for both the incident beam and fluorescence should be reduced. This can be challenging because the angle between the incident beam and the fluorescence detector is often mechanically fixed to 90° to reduce the background signal

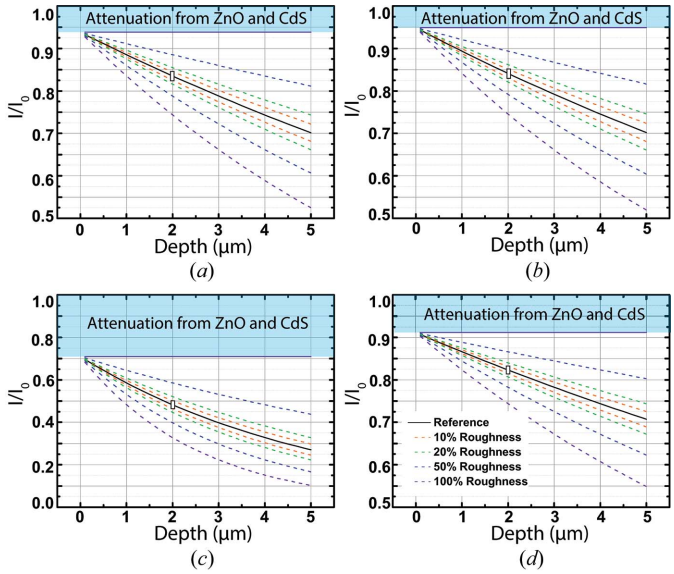

Figure 6
I/I_0 values for copper (*a*), gallium (*b*), indium (*c*) and selenium (*d*) as a function of the CIGS layer thickness for five different surface roughnesses, from ±10% of the film thickness to ±100% of the film thickness. The difference in scale for (*c*) should be noted when compared with (*a*), (*b*) and (*d*). The white box across the reference line at 2 μm in all panels represents a typical CIGS film with 10% surface roughness.

from scattered photons. This leads to a trade-off between the excitation volume of the beam and the path length of fluorescence. For a fixed detector/beam geometry of $\theta_{in} + \theta_{out} = 90°$, a good compromise is in many cases $\theta_{in} = 15°$. However, in an ideal case, $\theta_{in} = 0°$, such that a pixel in the map corresponds to the fluorescence signal of a perpendicular column in the sample [for a 2 μm-thick layer stack, an incident angle of 15° corresponds to the collection of fluorescence photons generated along $\tan(15°) \times 2\ \mu m = 536$ nm in the plane of the sample surface]. This is typically much wider than the spot size of the beam, which decreases the lateral spatial resolution given by the spot size.

It is important to note that although individually the sources of error may be small, when they are combined during the analysis they can result in non-negligible quantities, especially when handling multiple elements with low I/I_0 values, similar to indium in the case described above.

We have demonstrated a user-friendly method for the deconvolution of the effects of self-absorption and thickness variations inherent to many multicomponent layered structures, for use after XRF spectrum fitting and quantification. We have also performed a sensitivity analysis to estimate the potential sources of error and uncertainty when using the method for rough and compositionally graded samples. The applicability of this method was shown by the agreement between the data collected at two different APS beamlines under very different measurement geometries.

Although the data shown here are based on CIGS thin film solar cells, the process can be applied to any layered structure where surface roughness and compositional variations result in non-negligible error for the application. This process also enables the investigation of metal contaminants in silicon solar cells by estimating the depth of the detrimental particle. The investigation of fuel cells can be expanded to allow for *in situ* characterization of membrane contamination, by correcting for losses through the anode, cathode and membrane assembly. Therefore, the presented approach is a useful tool with broad-reaching impact across multiple disciplines, to be coupled with existing XRF analysis software, increasing the quantification accuracy, understanding areas of uncertainty and enabling the analysis of more complex samples.

Acknowledgements

The authors are grateful to Dr Harvey Guthrey and Dr Mowafak Al-Jassim at the National Renewable Energy Laboratory for providing CIGS solar cell samples. The authors also would like to acknowledge Professor David Fenning for fruitful discussions regarding the procedure presented. We would also like to thank Jake Vacek for assistance with graphic design and figure generation. Bradley West is supported by an IGERT-SUN fellowship funded by the National Science Foundation (award 1144616). We acknowledge funding from the US Department of Energy under contract DE-EE0005848. Use of the Advanced Photon Source and the Center for Nanoscale Materials, Office of Science user facilities, were supported by the US Department of Energy, Office of Science, Office of Basic Energy Sciences, under contract No. DE-AC02-06CH11357.

References

AXO Dresden (2015). *Thin Film XRF Reference Samples*, (http://www.axo-dresden. de/products/highprecision/reference.htm). Date accessed: 13 July 2016.
Beer, A. (1852). *Ann. Phys. Chem.* **162**, 78–88.
Berger, M. J., Hubbell, J. H., Seltzer, S. M., Chang, J., Coursey, J. S., Sukumar, R., Zucker, D. S. & Olsen, K. (2013). *NIST Standard Reference Database.* National Institute of Standards and Technology, Gaithersburg, MD, USA.
Bergmann, U. (2007). *Phys. World*, **20**, 39–42.
Bertoni, M. I., Fenning, D. P., Rinio, M., Rose, V., Holt, M., Maser, J. & Buonassisi, T. (2011). *Energ. Environ. Sci.* **4**, 4252.
Bleuet, P., Simionovici, A., Lemelle, L., Ferroir, T., Cloetens, P., Tucoulou, Ŕ. & Susini, J. (2008). *Appl. Phys. Lett.* **92**, 213111.
Brunetti, A., Golosio, B., Melis, M. G. & Mura, S. (2015). *Appl. Phys. A*, **118**, 497–504.
Buonassisi, T., Istratov, A. A., Pickett, M. D., Heuer, M., Kalejs, J. P., Hahn, G., Marcus, M. A., Lai, B., Cai, Z., Heald, S. M., Ciszek, T. F., Clark, R. F., Cunningham, D. W., Gabor, A. M., Jonczyk, R., Narayanan, S., Sauar, E. & Weber, E. R. (2006). *Prog. Photovolt. Res. Appl.* **14**, 513–531.
Casadio, F. & Rose, V. (2013). *Appl. Phys. A*, **111**, 1–8.
Chu, Y. S., Yi, J. M., De Carlo, F., Shen, Q., Lee, W. K., Wu, H. J., Wang, C. L., Wang, J. Y., Liu, C. J., Wang, C. H., Wu, S. R., Chien, C. C., Hwu, Y., Tkachuk, A., Yun, W., Feser, M., Liang, K. S., Yang, C. S., Je, J. H. & Margaritondo, G. (2008). *Appl. Phys. Lett.* **92**, 103119.
Contreras, M. A., Tuttle, J., Gabor, A., Tennant, A., Ramanathan, K., Asher, S., Franz, A., Keane, J., Wang, L., Scofield, J. & Noufi, R. (1994). *Proceedings of the 24th IEEE Photovoltaics Specialist Conference*, Waikoloa, HI, USA, pp. 68–75.
De Boer, D. K. (1990). *X-ray Spectrom.* **19**, 145–154.
De Jonge, M. D., Holzner, C., Baines, S. B., Twining, B. S., Ignatyev, K., Diaz, J., Howard, D. L., Legnini, D., Miceli, A., McNulty, I.,

Jacobsen, C. J. & Vogt, S. (2010). *Proc. Natl Acad. Sci. USA*, **107**, 15676–15680.
Delaney, G. W., Di Matteo, T. & Aste, T. (2010). *Soft Matter*, **6**, 2992–3006.
Dierolf, M., Menzel, A., Thibault, P., Schneider, P., Kewish, C. M., Wepf, R., Bunk, O. & Pfeiffer, F. (2010). *Nature (London)*, **467**, 436–439.
Fu, Y., Xi, Y., Cao, Y. & Wang, Y. (2012). *Phys. Rev. E*, **85**, 051311.
Grieken, R. van & Markowicz, A. A. (2002). *Handbook of X-ray Spectometry*, pp. 407–432. New York: Marcel Dekker.
Hu, Q., Aboustait, M., Ley, M. T., Hanan, J. C., Rose, V. & Winarski, R. (2014). *Acta Mater.* **77**, 173–182.
Huang, X., Yan, H., Nazaretski, E., Conley, R., Bouet, N., Zhou, J., Lauer, K., Li, L., Eom, D., Legnini, D., Harder, R., Robinson, I. K. & Chu, Y. S. (2013). *Sci. Rep.* **3**, 3562.
Hubbell, J., Trehan, P., Singh, N., Chand, B., Mehta, D., Garg, M. L., Garg, R. R., Singh, S. & Puri, S. (1994). *J. Phys. Chem. Ref. Data*, **23**, 339–364.
Karydas, A. G., Streeck, C., Bogdanovic Radovic, I., Kaufmann, C., Rissom, T., Beckhoff, B., Jaksic, M. & Barradas, N. P. (2015). *Appl. Surf. Sci.* **356**, 631–638.
Kienitz, B., Pivovar, B., Zawodzinski, T. & Garzon, F. H. (2011). *J. Electrochem. Soc.* **158**, B1175.
Krause, M. O. (1979). *J. Phys. Chem. Ref. Data*, **8**, 307.
Mainz, R. & Klenk, R. (2011). *J. Appl. Phys.* **109**, 123515.
Mukhopadhyay, S. & Peixinho, J. (2011). *Phys. Rev. E.* **84**, 011302.
Paunesku, T., Vogt, S., Maser, J., Lai, B. & Woloschak, G. (2006). *J. Cell. Biochem.* **99**, 1489–1502.
Ryan, C. G., Etschmann, B. E., Vogt, S., Maser, J., Harland, C. L., van Achterbergh, E. & Legnini, D. (2005). *Nucl. Instrum. Methods Phys. Res. B*, **231**, 183–188.
Sakdinawat, A. & Attwood, D. (2010). *Nat. Photon*, **4**, 840–848.
Schoonjans, T., Vincze, L., Solé, V. A., Sanchez del Rio, M., Brondeel, P., Silversmit, G., Appel, K. & Ferrero, C. (2012). *At. Spectrosc.* **70**, 10–23.
Solé, V., Papillon, E., Cotte, M., Walter, P. & Susini, J. (2007). *At. Spectrosc.* **62**, 63–68.
Streeck, C., Brunken, S., Gerlach, M., Herzog, C., Hönicke, P., Kaufmann, C. A., Lubeck, J., Pollakowski, B., Unterumsberger, R., Weber, A., Beckhoff, B., Kanngiesser, B., Schock, H.-W. & Mainz, R. (2013). *Appl. Phys. Lett.* **103**, 113904.
Tsukahara, M., Mitrovic, S., Gajdosik, V., Margaritondo, G., Pournin, L., Ramaioli, M., Sage, D., Hwu, Y., Unser, M. & Liebling, T. M. (2008). *Phys. Rev. E*, **77**, 061306.
Vogt, S. (2003). *J. Phys. IV Fr.* **104**, 635–638.
Vogt, S., Maser, J. & Jacobsen, C. (2003). *J. Phys. IV Fr.* **104**, 617–622.
Vyvenko, O. F., Buonassisi, T., Istratov, A. & Weber, E. R. (2004). *J. Phys. Condens. Matter*, **16**, S141.
West, B., Husein, S., Stuckelberger, M., Lai, B., Maser, J., Stripe, B., Rose, V., Guthrey, H., Al-Jassim, M. & Bertoni, M. (2015). *Proceedings of the IEEE Photovoltaic Specialist Conference (PVSC)*, New Orleans, LA, USA.
West, B. M., Stuckelberger, M., Guthrey, H., Husein, S., Lai, B., Maser, J., Stripe, B., Al-Jassim, M., Rose, V. & Bertoni, M. I. (2016). In preparation.
Winarski, R. P., Holt, M. V., Rose, V., Fuesz, P., Carbaugh, D., Benson, C., Shu, D., Kline, D., Stephenson, G. B., McNulty, I. & Maser, J. (2012). *J. Synchrotron Rad.* **19**, 1056–1060.
Yun, W., Lai, B., Cai, Z., Maser, J., Legnini, D., Gluskin, E., Chen, Z., Krasnoperova, A., Vladimirsky, Y., Cerrina, F., Di Fabrizio, E. & Gentili, M. (1999). *Rev. Sci. Instrum.* **70**, 2238.